

A CONSTRAINT ON THE ORGANIZATION OF THE GALACTIC CENTER MAGNETIC FIELD USING FARADAY ROTATION

C. J. LAW¹, M. A. BRENTJENS², AND G. NOVAK³

Draft version September 28, 2018

ABSTRACT

We present new 6 and 20 cm Very Large Array (VLA) observations of polarized continuum emission of roughly 0.5 square degrees of the Galactic center (GC) region. The 6 cm observations detect diffuse linearly-polarized emission throughout the region with a brightness of roughly 1 mJy per 15'' \times 10'' beam. The Faraday rotation measure (RM) toward this polarized emission has structure on degree size scales and ranges from roughly +330 rad m⁻² east of the dynamical center (Sgr A) to -880 rad m⁻² west of the dynamical center. This RM structure is also seen toward several nonthermal radio filaments, which implies that they have a similar magnetic field orientation and constrains models for their origin. Modeling shows that the RM and its change with Galactic longitude are best explained by the high electron density and strong magnetic field of the GC region. Considering the emissivity of the GC plasma shows that while the absolute RM values are indirect measures of the GC magnetic field, the RM longitude structure directly traces the magnetic field in the central kiloparsec of the Galaxy. Combining this result with previous work reveals a larger RM structure covering the central $\sim 2^\circ$ of the Galaxy. This RM structure is similar to that proposed by Novak and coworkers, but is shifted roughly 50 pc west of the dynamical center of the Galaxy. If this RM structure originates in the GC region, it shows that the GC magnetic field is organized on ~ 300 pc size scales. The pattern is consistent with a predominantly poloidal field geometry, pointing from south to north, that is perturbed by the motion of gas in the Galactic disk.

Subject headings:

1. INTRODUCTION

Diverse observations of the center of the Milky Way have found evidence for magnetic field strengths from 10–1000 μ G with both poloidal and planar geometries. Zeeman splitting of H I absorption lines shows that mG-strength magnetic fields exist in the central 2 pc (Plante et al. 1995). On the basis of their submillimeter polarimetric maps of the Galactic center region, Chuss et al. (2003) argue that molecular clouds in the central 100 pc have mG-strength fields oriented parallel to the plane of the Galaxy. At the same time, the detection of diffuse, polarized radio continuum emission implies that the central few hundred parsecs is permeated by magnetic field of strength 10 to 100 μ G (Haynes et al. 1992).

The most striking polarized structures in the GC region were discovered in radio continuum images: the nonthermal radio filaments (NRFs; Yusef-Zadeh et al. 1984). NRFs are long (several parsecs), polarized filaments found only in the central few degrees of our Galaxy and believed to be physically in the central few hundred parsecs (LaRosa et al. 2001; Nord et al. 2004; Yusef-Zadeh et al. 2004; Lasenby et al. 1989). Their tendency to align perpendicular to the Galactic plane shows that the GC region has some poloidal (i.e., vertical) magnetic field component with a local strength 1 mG (Yusef-Zadeh et al. 1997). This vertical structure is interesting in light of infrared polarimetry showing that the magnetic field tends to have a toroidal configuration in the plane, but

becoming poloidal at elevations above 0 $^\circ$:4 (Nishiyama et al. 2010).

Despite the wealth of observations, it has been difficult to merge these observations into a coherent model for the Galactic center (GC) magnetic field. How are the magnetic fields measured globally and locally related to each other (LaRosa et al. 2005; Ferrière 2009; Crocker et al. 2010)? What physical processes create the NRFs and determine their orientations (LaRosa et al. 2006)? Is the current state of the GC normal or does it represent a short phase of its evolution (Morris & Serabyn 1996; Law 2010)? Furthermore, the complexity of the range of polarimetric observations (some measure line-of sight field, some measure total field) argues for simulations to aid interpretation.

To understand the structure and strength of the GC magnetic field, we present new observations and modeling of the polarized continuum emission toward the GC region with the VLA. The observations were originally conducted in a study of the GC Lobe, a degree-tall, loop-like structure spanning the central degree of the GC region (Sofue & Handa 1984; Bland-Hawthorn & Cohen 2003; Law 2010). In § 2, the observations are described; § 3 discusses some of the techniques used to analyze the polarized emission. This survey is the largest-area, interferometric survey of diffuse polarized emission ever done in the GC region. Section 4 describes the detection of extended, polarized emission throughout the region and the large-scale rotation measure (RM) structure seen towards it. Section 5 uses the observed RM to constrain a simple model of the Galaxy's electron density and magnetic field. Modeling of the emission and Faraday rotation argues that the GC magnetic field geometry is predominantly poloidal with a perturbation by motion

¹ Radio Astronomy Lab, University of California, Berkeley, CA, USA; claw@astro.berkeley.edu

² ASTRON, Dwingeloo, Netherlands

³ Department of Physics and Astronomy, Northwestern University, Evanston, IL, USA

of gas in the disk of the Galaxy.

2. OBSERVATIONS AND DATA REDUCTION

Between January and August of 2004, we surveyed the GC region with the VLA at 6 cm in the DnC configuration and at 20 cm in the CnB, DnC, and D configurations. The goal of the observation was to create wide-field mosaics of the GC lobe, as described in Law et al. (2008a). That paper presents catalogs of discrete polarized and unpolarized sources in the survey; extended polarized emission, particularly at 6 cm, is discussed here. The 6 cm observations covered roughly half a square degree from $l = 359^{\circ}2$ to $0^{\circ}2$, $b = 0^{\circ}2$ to $0^{\circ}7$. Critically for the present work, the default continuum mode observed with two, adjacent 50 MHz bands centered at 4.835 and 4.885 GHz.

Observations of J1751-253 were used for phase calibration, while J1331+305 (3C 286) was used for flux calibration. Observations of the unpolarized phase calibrator covered a parallactic angle range of 80° . This is wide enough to measure receiver “leakage”, the detection of left-circular polarization by the right-circular receiver and vice versa (Cotton 1999). After applying the leakage corrections to the scan of 1331+305, the phase delay between left and right polarizations was set to produce the known polarization angle of 66° .⁴

Images were produced with AIPS⁵ using both the multi-resolution and the standard CLEAN algorithms. The resulting mosaics and derived properties were similar within their errors. The final mosaics presented here were deconvolved with a multi-resolution CLEAN algorithm. The Stokes Q and U images were cleaned independently with resolutions of 1, 3, and 9 times the beam size to produce a single image per Stokes parameter. The entire primary beam was cleaned until the maximum residual brightness was less than the noise level outside the primary beam. The same number of iterations was used to clean both bands. Images were restored with a single beam of size $15'' \times 10''$ with PA = 70° , which is representative of the whole mosaic.

The Stokes Q and U images were subsequently primary-beam corrected and combined to form mosaics for each band. Figure 1 shows the polarized intensity mosaic after averaging over both bands. The polarized intensity is visible on scales of a few arcminutes because it is laced with depolarized “canals” (Wieringa et al. 1993; Yusef-Zadeh et al. 1986; Haverkorn et al. 2004). Figure 2 shows an example of canals in the polarized emission in the eastern half of the survey.

To correct for noise bias in maps of polarized emission, a noise mosaic was constructed by quadratically adding noise images from each field. A noise image was created for each field by applying the primary beam correction to an image with each pixel value set to the image noise. The noise level for each field was measured outside the primary beam, since the image centers are filled with emission. Observed noise values range from 50 to 120 μ Jy. The observed noise is a factor of 2–4 times higher than the theoretical sensitivity, which is consistent with the expected additional noise from sidelobes and calibration errors. Finally, mosaics of polarized intensity,

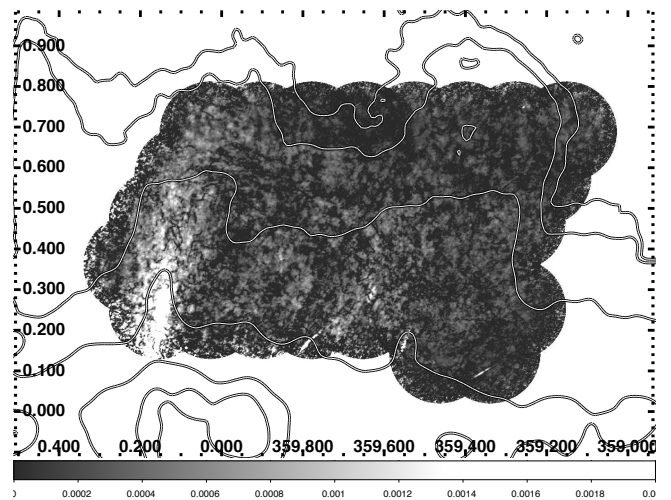


FIG. 1.— Mosaic of 6 cm polarized intensity observed in 42 VLA pointings with contours of 6 cm total intensity from the GBT with Galactic coordinates (Law et al. 2008b). The beam size is $15'' \times 10''$ with a position angle of 70° . Gray scale shows VLA 6 cm polarized intensity from 0 to 2 mJy beam⁻¹ as indicated on the colorbar in units of Jy. Contours show GBT 6 cm brightness at $33 \times 3''$ mJy per $150''$ circular beam, for $n = 0 - 4$. Most of the polarized emission seen is significant.

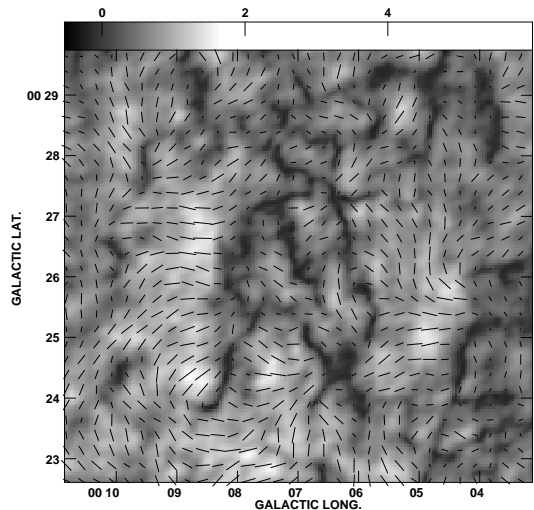


FIG. 2.— Map of the 6 cm polarized intensity near the eastern edge of the survey, where depolarized “canals” are evident. The lines show the polarization angle of the emission at 4.835 GHz. The polarization angle changes by 90° across the canals, indicating depolarization within the beam by small-scale changes in the Faraday-rotating medium (Haverkorn et al. 2004).

position angle, and their associated errors were created for each band.

Leakage calibration is most valid at the phase center, as errors are known to increase away from there. The VLA position-dependent leakages are based in the antenna and induce a false linear polarization that is radially oriented (Cotton 1994, 1999). The magnitude of the false polarization is roughly 3% of Stokes I at the full-width at half-max (FWHM) of the primary beam at 1.4 GHz. It is not measured at other frequencies, but we

⁴ See <http://www.vla.nrao.edu/astro/calib/manual/polcal.html>; R. Perley & N. Killeen, private communication

⁵ See <http://www.aips.nrao.edu>

use 3% as a rough estimate of errors at 5 GHz. Since this error is antenna based, our observations covering a parallactic angle range of 80° reduces the effect by about 30%. More importantly, the diffuse polarized emission discussed in this work has no total intensity counterpart, so errors in Stokes Q and U scale with Stokes Q and U, instead of Stokes I (Sault et al. 1996). Furthermore, measurements of RM are not biased by the leakage, but the change in leakage with frequency, which tends to be smaller. Considering all these effects, we expect position-dependent leakage errors to be less 3% of Stokes Q and U, less than the typical flux calibration errors and unlikely to affect the results presented here. Section 3.2 compares our results to previous GC polarimetry observations and generally confirms this assumption.

Finally, it is important to consider the fact that interferometric observations are not sensitive to emission on large angular scales (Haverkorn et al. 2004; Schnitzeler et al. 2009). Missing Q and U flux can create spurious polarization and bias RM values. Haverkorn et al. (2004) show that a wide distribution of RM randomizes any uniform polarized background and reduces the missing flux. The RM distribution observed here (described in detail in § 3.1) has a width of about 500 rad m^{-2} on size scales used in this study ($>100''$), which limits the missing flux to less than 0.2%. As an alternative derivation of missing flux, Schnitzeler et al. (2009) show that a gradient in RM can shift the spatial scale at which polarized emission is visible. For the RM gradient seen here ($\approx 5 \text{ rad m}^{-2} \text{ arcsec}^{-1}$), that technique predicts a shift in spatial scales from zero to about 1200λ , larger than our shortest baseline. Both techniques indicate that an insignificant amount of polarized flux is missed by the present observations.

3. ANALYSIS

3.1. Polarization Angle Difference Across Bands

To study the RM across this field, mosaics of the polarization angle were differenced between the two bands. The polarization angle difference image (hereafter $\Delta\theta$ image) was created by differencing the polarization angle images ($\theta_{4.885\text{GHz}} - \theta_{4.835\text{GHz}}$) and remapping each value of $\Delta\theta$ to the range -90° to 90° . Figure 3 shows the $\Delta\theta$ image and its error. Observationally, the rotation measure is defined as $\text{RM} = \Delta\theta / \Delta(\lambda^2)$. Assuming this λ^2 law, a position angle difference of 1° corresponds to a rotation measure of -220 rad m^{-2} .

More generally, the observed polarization is the sum of polarized emission emitted with a range of RM (Burn 1966; Brentjens & de Bruyn 2005). Such complex sources can have non-quadratic changes in the polarization angle that can confuse a simple analysis. In these situations, the pertinent physical quantity is the ‘‘Faraday depth’’:

$$\phi = 0.81 \int_{\text{there}}^{\text{here}} n_e \vec{B} \cdot d\vec{l} \text{ rad m}^{-2}, \quad (1)$$

where n_e is in cm^{-3} , \vec{B} is in G, and $d\vec{l}$ is in pc. For simple physical distributions of n_e and \vec{B} , ϕ is equal to RM. However, robustly tying the RM to physical conditions in complex cases requires measurements at many wavelengths (Brentjens & de Bruyn 2005). Since we only have two wavelengths to study the polarization in this region, we instead use this formalism to define the limits of deriving physical conditions from the observed RM.

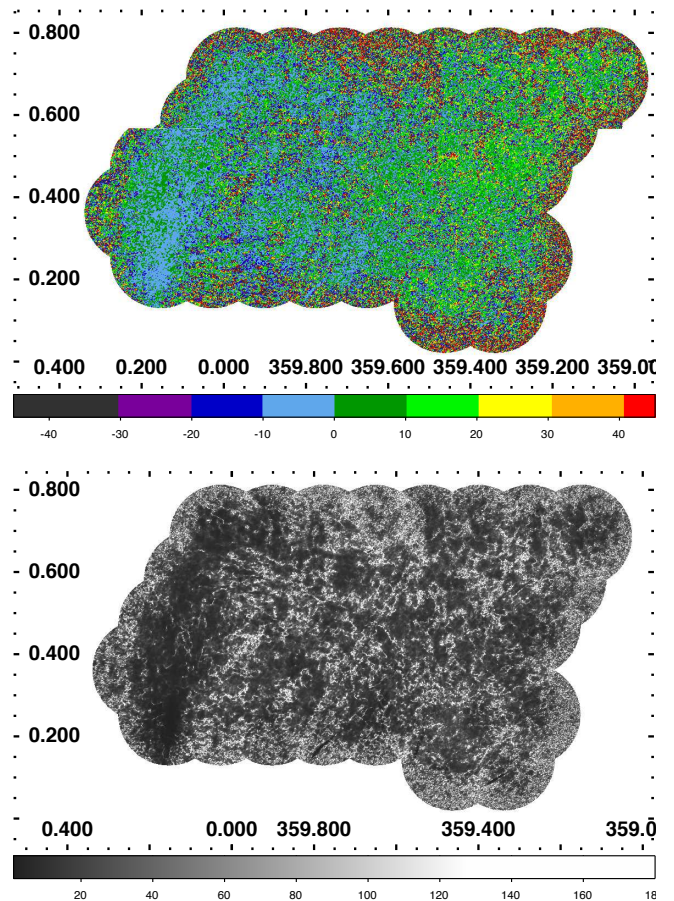


FIG. 3.— *Top*: Map of the polarization angle difference, or $\Delta\theta$, for the 6 cm survey of the GCL. The color scale is linear according to the colorbar at the bottom in units of degrees; 1° is equivalent to a RM of -220 rad m^{-2} . The edges of the map have large values of $\Delta\theta$ because the sensitivity is low there. *Bottom*: Map of the error in $\Delta\theta$. The greyscale is linear, with values ranging from 1° to 180° . The typical error in the $\Delta\theta$ value is about 5° .

First, the formalism of Brentjens & de Bruyn (2005) shows that the spacing of the bands in wavelength determines the ‘‘RM resolution’’ and possible $n\pi$ ambiguities. For the two bands used here, the RM resolution is $4 \times 10^4 \text{ rad m}^{-2}$ and any aliasing occurs at $\text{RM} = n * 4 \times 10^4 \text{ rad m}^{-2}$, for an integer n . The RM expected in the GC region covered by this survey is typically $< 2000 \text{ rad m}^{-2}$ (Yusef-Zadeh et al. 1984; Tsuboi et al. 1986; Roy et al. 2005), so there is little chance of an $n\pi$ ambiguity. Second, the bandwidth determines the amount of Faraday rotation within a band, which limits the maximum Faraday depth detectable to $\phi < 2 \times 10^4 \text{ rad m}^{-2}$. Finally, a source that emits over a range of Faraday depths, known as ‘‘Faraday thick’’, can be internally depolarized. The maximum Faraday thickness detectable to the present observations is 830 rad m^{-2} . Some sources, such as the Radio Arc (Yusef-Zadeh & Morris 1987, 1988), have an RM that changes by more than 830 rad m^{-2} , so parts of the GC region may be Faraday thick to our observations.

Figure 4 shows histograms of $\Delta\theta$ (number of independent spatial beams per degree of $\Delta\theta$) from the entire survey and a smaller region. Intrinsically, we expect the $\Delta\theta$ histogram to have contributions from many distinct regions of varying peak $\Delta\theta$ and width. We found that

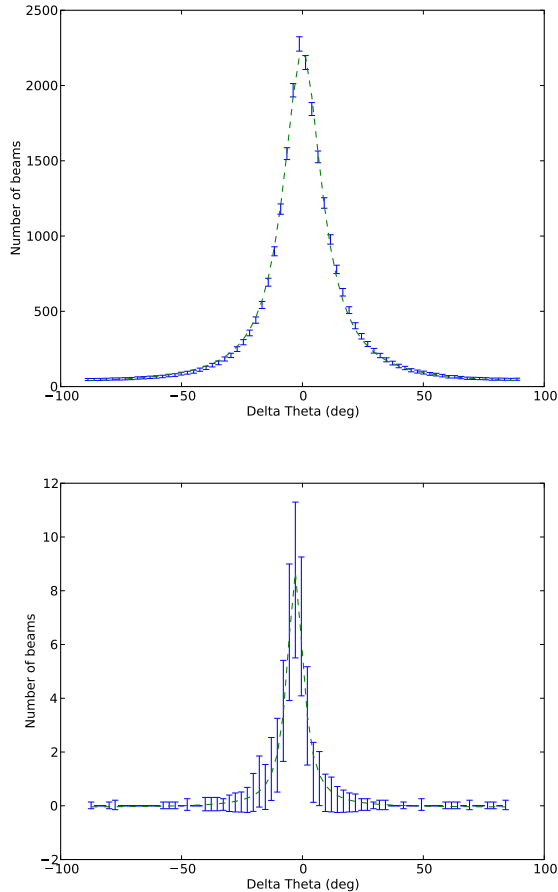


FIG. 4.— *Top*: Histogram of $\Delta\theta$ in each independent beam in the survey region. The blue error bars show the $\Delta\theta$ values assuming they follow a Poisson distribution and uses a bin size of $2^{\circ}5$ of $\Delta\theta$. The green dashed line shows the best-fit Lorentzian model, which has a peak of 2200 beams per degree, a half-width of about 10° , and a constant background of about 13 beams per degree of $\Delta\theta$. *Bottom*: A similar plot as shown at top, but for a $125'' \times 125''$ box in the eastern half of the survey. This histogram shows the amount of data in each pixel of the smoothed maps shown below.

a Lorentzian profile fits these heterogeneous distributions better than a single Gaussian. For smaller regions, where $\Delta\theta$ has a single-valued, noise-like distribution, the Lorentzian can also approximate a single Gaussian. In the limit of a single-valued, noise-like $\Delta\theta$ distribution, the Gaussian noise is equivalent to a Poisson distribution in the large- N limit. We use this similarity to approximate the $\Delta\theta$ bin count errors as $\sigma_N = 1 + \sqrt{N + 0.75}$, where N is the number of independent beams in a bin (Gehrels 1986). In §3.2, we show that comparing RM measured histogram methods to previous work shows that the errors are conservative.

Aside from theoretical expectations, the distribution of $\Delta\theta$ values shows that the apparent $\Delta\theta$ can generally be reliably converted to RM. Most values of $\Delta\theta$ measured have small offsets from 0° , with $\sim 50\%$ within $\pm 10^{\circ}$, $\sim 75\%$ within $\pm 20^{\circ}$, and $\sim 90\%$ within $\pm 45^{\circ}$. This is consistent with the $\sim 9^{\circ}$ rotation expected for $\text{RM} \approx \pm 2000 \text{ rad m}^{-2}$. The typical angle change is $\ll 1 \text{ rad}$, so relative angles may be treated as roughly linearly distributed. The best constraint on the mean $\Delta\theta$ has a typical error of about 1° , or 220 rad m^{-2} . For a change of 1° between

our two bands, the Faraday rotation from $\lambda = 0 \text{ cm}$ is 49° . This typical uncertainty in $\Delta\theta$ makes the calculation of the intrinsic polarization angle highly uncertain, so no such results are presented here.

Visualizing the images of $\Delta\theta$ and RM is difficult, since the per-pixel sensitivity is poor and varies across the field of view. Convolution and other image processing techniques can be used to extract this information even in poorly-calibrated VLA data (Rudnick & Brown 2009). We tested two statistical techniques to spatially smooth the RM: averaging and histogram fitting. These methods and a comparison of their results are described in Appendix A. In general, the two methods have similar results. The histogram-fitting method is less sensitive to outliers and has more conservative errors, so it is used in all results described below.

3.2. Comparison to Earlier Work

Since this work is applying a relatively new technique to a complex region, it is important to test the results against known sources. This section compares our results shown in Figures 1 and 3 to the RM for specific regions studied previously (LaRosa et al. 2001; Tsuboi et al. 1986; Haynes et al. 1992; Roy et al. 2005; Yusef-Zadeh et al. 1997). LaRosa et al. (2001) present images of 6 cm polarized intensity near the nonthermal radio filament G359.85+0.39 from VLA data with similar sensitivity and resolution as the present study. The two surveys have similar brightness distributions and structure in the polarized emission, particularly the depolarized regions on the southeast and northeast sides of G359.85+0.39 (see also Law et al. 2008a). The similarity shows that the calibration and imaging quality is similar to that of LaRosa et al. (2001).

Haynes et al. (1992) and Tsuboi et al. (1986) conducted independent, single-dish surveys near 3 cm, covering a few square degrees of the GC region. Although depolarization is weaker near 3 cm and their beam is larger, there is general agreement between our Figure 1 and their polarized intensity maps. Figure 5 shows a comparison of our RMs with the four-band measurements of Tsuboi et al. (1986). Near $(0^{\circ}17, 0^{\circ}22)$ and $(0^{\circ}1, 0^{\circ}35)$, Tsuboi et al. (1986) find the RM has a maximum of $+1000 \text{ rad m}^{-2}$, while the present survey finds a maximum of $770 \pm 110 \text{ rad m}^{-2}$. The maps are similar moving north across $(0^{\circ}15, 0^{\circ}4)$, where the RM switches from positive to negative values; Tsuboi et al. (1986) measure $\text{RM} \approx -250 \text{ rad m}^{-2}$ while the present survey finds $-220 \pm 130 \text{ rad m}^{-2}$. There is some agreement at the northwestern edge of the polarized emission of the Radio Arc, shown in Figure 5, where the RM switches back to positive values. The exact location of this second RM sign change is slightly different and may reflect the different RM depths each survey is sensitive to.

Yusef-Zadeh et al. (1997) presented a detailed study of the polarization properties of the nonthermal filament G359.54+0.18 (RF-C3) at 6 and 3.6 cm. Figure 3 of that work has a similar 6 cm brightness and RM distribution as the present work, both presented here and in Law et al. (2008a). The RM map of the filament shows three distinct, bright clumps each having relatively uniform values. The morphology seen in the present survey is similar to that of Yusef-Zadeh et al. (1997), although it had roughly three times better resolution ($4''$ compared

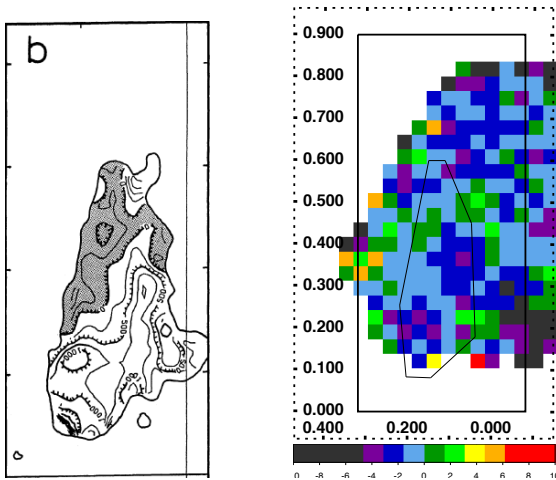


FIG. 5.— *Left*: Reprint of Fig. 4 from Tsuboi et al. (1986) showing the RM for the northern extension of the Radio Arc, as observed by the Nobeyama Radio Observatory near 3 cm with a beam size of $2.7''$. The contours show steps of 250 rad m^{-2} , with the shaded region showing negative RM and unshaded region showing positive RM. *Right*: $\Delta\theta$ image from the present 6 cm, VLA survey smoothed by the histogram-fitting method with $125'' \times 125''$ boxes. The colorbar shows the $\Delta\theta$ value in units of degrees. The rectangle shows the extent of the left figure on this figure and the irregularly-shaped box schematically shows the outermost contour from the left figure.

to $12''$ in the present work). The first clump, at RA, Dec (B1950) = (17:40:41, $-29:12:30$) has $\text{RM} \approx -2700 \text{ rad m}^{-2}$, compared to $-3960 \pm 1100 \text{ rad m}^{-2}$ in the present survey. The second clump, at (17:40:43, $-29:12:40$), has $\text{RM} \approx -2000 \text{ rad m}^{-2}$, compared to $-2200 \pm 440 \text{ rad m}^{-2}$ in the present survey. The third clump, at (17:40:44, $-29:12:45$), has $\text{RM} \approx -1500 \text{ rad m}^{-2}$, compared to $-1540 \pm 660 \text{ rad m}^{-2}$ in the present survey. We conclude that, in general, there is good agreement between the RM of the present survey and that of Yusef-Zadeh et al. (1997).

In summary, the polarized intensity and RM of the present 6 cm survey shows good agreement with those of other surveys. This is consistent with the fact the polarimetric leakage is expected to have relatively little frequency structure for the VLA feed design (Cotton 1994, 1999); any systematic errors in the polarization angle are subtracted when forming the $\Delta\theta$ image. It also shows that histogram fitting of the $\Delta\theta$ values is a reasonable estimate of the RM and its uncertainty at 6 cm in this region.

4. RESULTS

4.1. Extended Polarized Emission

The 6 cm polarized continuum intensity of the northern extension of the Radio Arc is several mJy beam^{-1} and spans the entire eastern edge of the survey up to a latitude of $b \sim 0^\circ.8$. To test for frequency structure in the polarized intensity, the polarized intensity maps in the two bands were differenced. The lack of diffuse emission in the difference map shows that the two maps have similar diffuse emission within roughly 1 mJy . The comparable 20 cm mosaic of polarized continuum shows no extended emission down to a level of about $0.1 \text{ mJy beam}^{-1}$ (more detail in Law et al. 2008a).

For latitudes up to $b = 0^\circ.3$, the polarized continuum

emission seen in the 6 cm interferometric maps (Fig. 1) has a total intensity counterpart in the same data. However, north of $b = 0^\circ.3$, the total intensity counterpart is too extended to be detected by the VLA 6 cm observations. Since the polarized emission is broken into small spatial scales (as shown in Figure 2), it is detected throughout the region and the apparent polarization fraction often exceeds 100%.

To estimate the polarization fraction without the effect of missing flux, we compare the VLA polarized-intensity maps to continuum maps from the Green Bank Telescope (Law et al. 2008b). We convolve the VLA maps to the GBT resolution to estimate the polarization fraction; this will be a lower limit, since the VLA emission is laced with depolarized canals. At 6 cm, the peak polarization fraction is 25% in the eastern half of the survey and 10% in the western half of the survey. These values are consistent with other single-dish surveys (Tsuboi et al. 1986; Haynes et al. 1992), which confirms the validity of techniques and maps of the VLA survey. At 20 cm, the upper limit on the polarization fraction is roughly 1% of the total intensity measured by the GBT.

4.2. Degree-scale RM Structure

Figure 6 shows two maps of RM smoothed over 125 -arcsec tiles with the histogram-fitting method. The images show there is coherent structure on degree size scales. The east side of the survey tends to have RM greater than zero and the west side less than zero.

The east-west structure is seen more clearly in averages calculated over all latitudes, as shown in Figure 7. In the east, for $0^\circ.2 < l < -0^\circ.3$, $\text{RM} \approx +330 \text{ rad m}^{-2}$, then the RM changes rapidly for $-0^\circ.3 < l < -0^\circ.55$, and in the west, for $-0^\circ.95 < l < -0^\circ.55$, $\text{RM} \approx -880 \pm 50 \text{ rad m}^{-2}$. Averaging RM over the top half of the survey ($0^\circ.45 < b < 0^\circ.7$) shows a similar structure as the average over all latitudes, but with a larger range. The maximum RM is $+660 \pm 75 \text{ rad m}^{-2}$ near $l = -0^\circ.25$ on the east side, while the minimum RM is $-1320 \pm 75 \text{ rad m}^{-2}$ near $l = -0^\circ.65$ on the west side.

4.3. Localized Features in the RM Image

There are three arcminute-scale RM features that deviate from the simple structure described above. One of the regions with the largest positive RM is at the southern border of the survey, near $(-0^\circ.1, 0^\circ.2)$. Figure 8 shows that the region with large RM covers a region about $8'$ across, just north of Sgr A. The average RM for this region is $+188 \pm 198 \text{ rad m}^{-2}$. The average RM for all latitudes near $l = -0^\circ.1$ is $\approx +330 \pm 60 \text{ rad m}^{-2}$.

The region with the most negative RM is at $(-0^\circ.6, +0^\circ.5)$, on the right side of Figure 6. Over an area about $8'$ across, the mean RM is $-1320 \pm 110 \text{ rad m}^{-2}$. Figure 7 shows that the mean RM at $l \sim -0^\circ.6$ is $\approx -880 \pm 110 \text{ rad m}^{-2}$. This feature may partially explain why the amplitude of the east-west RM asymmetry is larger when averaging over the top half of the survey.

A third unusual RM structure is a ridge extending from $(0^\circ.25, +0^\circ.4)$ to $(0^\circ.0, +0^\circ.5)$, seen at the left of Figure 6. The feature has a negative RM, but the surrounding region has a positive RM. The average RM along this ridge is $\approx -220 \pm 110 \text{ rad m}^{-2}$, as compared to the mean value of $\approx 330 \pm 60 \text{ rad m}^{-2}$ for all latitudes near $l = 0^\circ$. This structure is seen in the RM map of Tsuboi et al. (1986),

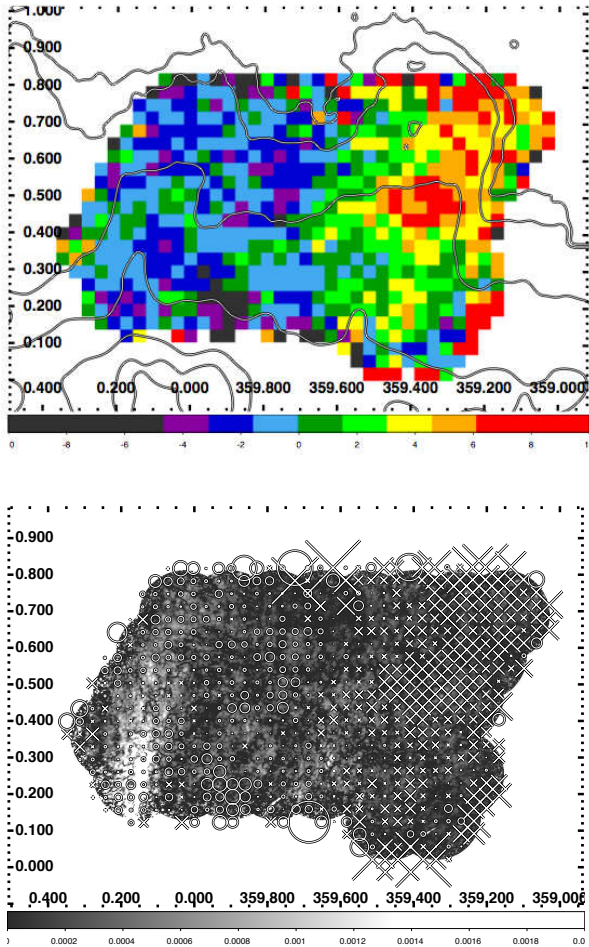


FIG. 6.— *Top*: Map of $\Delta\theta$ at 6 cm averaged over 125-arcsec tiles with the histogram-fitting method in units of degrees. The contours show 6 cm brightness as observed by the GBT, similar to Fig. 1, with levels of $33 * 3^n$ mJy per $150''$ beam, with $n = 0 - 5$. *Bottom*: Gray scale shows the 6 cm polarized intensity from 0 to 2 mJy, as in Fig. 1. The symbols show the smoothed RM, assuming -220 rad m^{-2} per $\Delta\theta$ in the top panel. Crosses show positions with $RM < 0$ and circles showing $RM > 0$. The size of the symbol is proportional to RM and ranges from -5720 to 4180 rad m^{-2} .

and a detailed comparison of that work to the present work is shown in Figure 5.

5. DISCUSSION

5.1. Modeling the Rotation Measure

The complexity of the line of sight to — and through — the GC region argues for caution when interpreting RM patterns. The apparent 6 cm RM suggests that the line of sight magnetic field changes sign, as if the field was predominantly azimuthal. However, it is not immediately clear whether the observed polarized emission originates in the GC region or whether the observed RM can be used to measure properties of the GC magnetic field. This section addresses these issues with modeling of the Galactic electron density and magnetic field. We use the observed 6 cm RM longitude dependence to constrain parameters of the model and ultimately derive the expected polarimetric properties of the region over a range of wavelengths.

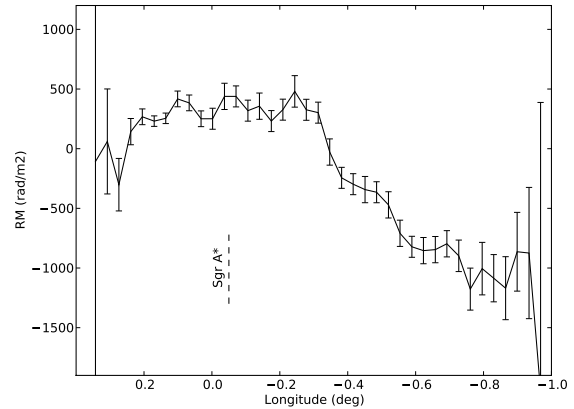


FIG. 7.— The RM at 6 cm as a function of Galactic longitude, assuming 1° of $\Delta\theta$ is equal to -220 rad m^{-2} . The RM and its error are found by the histogram-fitting method for the entire latitude range of the survey ($0^\circ 1 < b < 0^\circ 8$) in strips of width $125''$. The longitude of Sgr A*, the dynamical center of the Galaxy, is shown with a dashed line.

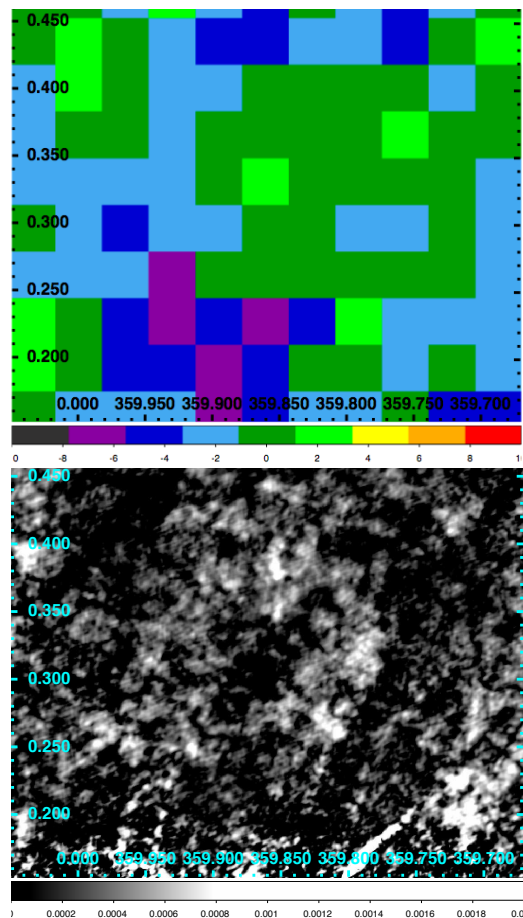


FIG. 8.— *Top*: Smoothed map of $\Delta\theta$ in units of degrees for the region near the region of large negative $\Delta\theta$. *Bottom*: Map of the 6 cm polarized intensity for the same region as in the top panel. The gray scale shows brightness ranging from 0 to 1 mJy $beam^{-1}$. The NRF called the Cane (LaRosa et al. 2001) is located at the top of the loop at $(359^\circ 85, 0^\circ 39)$.

5.1.1. Galactic Model

The RM is calculated from a model of the electron density, n_e , and the Galactic horizontal magnetic field, \vec{B} . We use a cartesian Galactic coordinate system with the origin at $l = 0^\circ$ at a distance of r_{GC} from the Sun, the x axis pointing towards negative l , the y axis pointing away from the Sun, and the z axis pointing to positive b . This technique does not calculate the emissivity of the synchrotron radiation, so we effectively assume that the polarized emission originates behind the Faraday rotating medium on the xz -plane. The integral is done along a line to the GC distance, so the polarized emission is assumed to be at the peak of the electron distribution. For this model, the Faraday depth along a given line of sight is:

$$\phi = \phi_0 + 0.81 \int_{r_{GC}-5w}^{r_{GC}} n_e \vec{B} \cdot d\vec{r}, \quad (2)$$

where ϕ_0 is the foreground Faraday depth, r is the distance from the Sun along the line of sight, and w is the horizontal FWHM of the Galactic Center electron density enhancement (Cordes & Lazio 2002). As described below, the Faraday rotation induced by the GC region dominates, so the limits of integration include only a path of length $5w$ on the front side of the GC. In §5.1.3, we relax this assumption and consider the emissivity of the plasma. The model electron density is:

$$n_e \exp \left\{ -4 \log 2 \left[\frac{(x-x_0)^2 + (y-y_0)^2}{w^2} + \frac{(z-z_0)^2}{h^2} \right] \right\}, \quad (3)$$

where n_d represents the electron density of the disc, excluding the Gaussian enhancement in the Galactic center. Here n_d is assumed constant throughout the volume. The central enhancement is described by a three-dimensional Gaussian function, where x_0 , y_0 , and z_0 are its offset, h is its vertical FWHM, and n_0 is its maximum density.

Since the model is fit to RM measurements, the magnetic field model describes only the horizontal component. The field points counter-clockwise as seen looking down on the plane, with the pitch angle p pointing slightly outward for positive p . The horizontal field strength is assumed to be a constant, b_0 .

$$\mathbf{B}(x, y, z) = |b_0| \begin{pmatrix} -\sin(\theta - p) \\ \cos(\theta - p) \\ 0 \end{pmatrix}, \quad (4)$$

where

$$\theta = \tan^{-1} \frac{y - y_0}{x - x_0}. \quad (5)$$

5.1.2. Model Fit

The 11 model parameters must be estimated carefully: there are only 39 longitude bins over a narrow l , b range and only 2 frequency channels. To simplify the procedure, we only solve for four parameters: foreground RM, x -offset, magnetic field strength, and pitch angle. The parameters r_{GC} , w , h , n_0 , y_0 , and z_0 have default values taken from NE2001 (Cordes & Lazio 2002), while the disc electron density, n_d , is the sum of the NE2001 thin

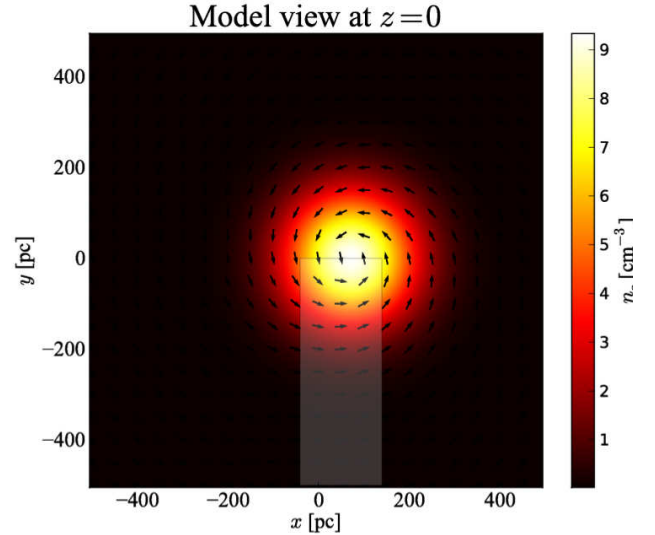


FIG. 9.— Electron density and magnetic field in the plane of the Galaxy for the best-fit model. For the least squares fit, the model was evaluated in the lightly shaded box at $b = +0^\circ.5$ or $z \approx +55$ pc. The model parameters are listed in Table 1.

disc and the Gaensler et al. (2008) thick disc, evaluated at the Galactic center. These default parameter values, shown in Table 1, are consistent with other observations (Spangler 1991; LaRosa et al. 2005; Lazio & Cordes 1998; Han et al. 2006).

Figure 9 shows a top-down view of the spatial distribution of the electron density and magnetic field. The shaded region demonstrates that the observed area is rather small compared to the model structure. This shows that the observations are limited to the center of the electron distribution.

We determine the best-fit parameter values and uncertainties with a three-step Monte-Carlo method. First, we randomly generate a list of 4000 mock observations. The RM value at each l is drawn from a Gaussian distribution with mean and standard deviation equal to the RM and its error measured over the entire latitude range of the survey (as shown in Figure 7). Second, we fit Equation 2 for $b = +0^\circ.5$ to each mock data set by minimizing the reduced χ^2 using the nonlinear, constrained, L-BFGS-B solver (Zhu et al. 1994). Third, the mean and standard deviation of each parameter is measured from the ensemble of fit results.

The parameters and fit results for the longitude dependence of the 6 cm RM are summarized in Table 1. Figure 10 shows the 68% and 95% confidence levels for all pairs of variables. The foreground RM is orthogonal

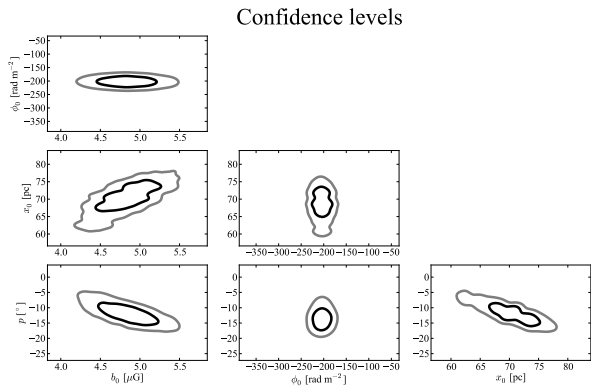


FIG. 10.— Confidence levels for all pairs of variable parameters. The 68% confidence level contour is black, the 95% confidence level contour gray.

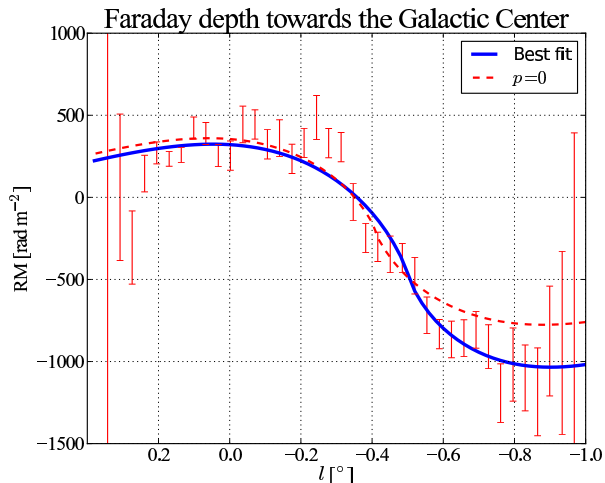


FIG. 11.— The 6 cm RM as a function of Galactic longitude in the GC region. The solid blue line shows the observed RM, measured over the entire latitude range of the survey ($0^\circ.1 < b < 0^\circ.8$). The dashed red line shows the best-fit model at the mean latitude of the survey ($+0.5^\circ$; parameters shown in Table 1).

to all other parameters, while the remaining three show mild degeneracies.

The 6 cm RM predicted by the best-fit model is compared to the observed RM in Figure 11. Since the geometry of the magnetic field is not well known in the GC region, we compare the observations to the best-fit model with and without a pitch angle parameter. For the model with the pitch angle (and shown in Table 1), the reduced χ^2 is 1.6 with 34 degrees of freedom. The model with no pitch angle parameter is slightly worse, particularly at $l < -0.6^\circ$, with a reduced χ^2 of 2.2 and 35 degrees of freedom. A p of 0 is ruled out formally at the 3σ level, although as discussed in §5.1.3 considering emissivity of the model will change some details of the best-fit parameters.

The quality of the fit shows that a realistic GC electron distribution and magnetic field geometry can explain the observed RM longitude pattern. In particular, the rapid

change of RM with Galactic longitude is best explained by the rapidly changing magnetic field orientation within the central few hundred parsecs. This is consistent with our assumption that most of the polarized emission originates in the center and that the Faraday rotation happens on the near side of the GC.

Not only can the model fit the observed RM pattern, but the best-fit values are consistent with other observations. The magnetic field strength and electron density are degenerate in the model, but we constrain the horizontal component of the magnetic field to be roughly $5(10 \text{ cm}^{-3}/n_e^{\text{gc}})\mu\text{G}$ at heights of about 0.5° . Considering the predominantly vertical orientation of the magnetic field (Nishiyama et al. 2010), the implied total field strength is consistent with that measured previously (Haynes et al. 1992; Ferrière 2009; Crocker et al. 2010). The foreground RM is similar in magnitude to that observed toward the pulsars in the inner Galaxy, which have RM up to $\sim 200 \text{ rad m}^{-2}$ (Manchester et al. 2005; Han et al. 2006). We compare this model to other measurements of the foreground RM in §5.3.

The physical consistency of the model to GC region argues for a GC origin of the polarized emission. The shape of the RM distribution requires a value of $n_e \cdot B_{\parallel}$ that exists only in the GC region (Lazio & Cordes 1998). Also, the typical n_e and B_{\parallel} in the Galactic plane are not changing enough with longitude to cause the observed RM pattern.

5.1.3. Faraday Depth Estimate

While the model is based on the observed 6 cm RM, reasonable assumptions about the synchrotron emission in our volume will allow us to predict RM and depolarization at all frequencies and positions. These assumptions are not parameterized in our initial model fit, so its predictions can comment on the reasonableness of our model. Below we show how the model predicts a Faraday depth distribution and how it affects the interpretation of the observed polarization at 6 cm.

The following treatment of synchrotron radiation closely follows that of Sun et al. (2008). The synchrotron intensity of a slice with thickness $d\vec{r}$ is given by

$$I d\vec{r} \propto n_{\text{rel}} \vec{B}_{\perp}^2 \nu^{-1} d\vec{r}, \quad (6)$$

where n_{rel} is the relativistic electron density. We assume that n_{rel} is constant in the inner 3 kpc of the Milky Way, that the intrinsic fractional polarization of each volume element is constant in frequency and space, and that the shape of the synchrotron spectrum is the same in all volume elements. We therefore drop the frequency dependence and relativistic electron density from our simulation of the polarized intensity:

$$f I d\vec{r} \propto \vec{B}_{\perp}^2 d\vec{r}, \quad (7)$$

where f is the fractional polarization. If the magnetic energy density is equal to the gas energy density, then, according to Murgia et al. (2004),

$$\|\vec{B}\| \propto n_e^{1/2}. \quad (8)$$

Because $\|\vec{B}\|$ is likely an order of magnitude stronger than the horizontal field (Crocker et al. 2010), we assume for the sake of simplicity that $B_{\perp} \approx \|\vec{B}\|$, and therefore

TABLE 1
MODEL PARAMETERS

Name	Value	\pm	Unit	Range ^a	Description
b_0	4.84	0.25	μG	[0.1, 20]	Magnetic field strength in plane
p	-11.6	3.9	$^\circ$	[-25, 25]	Pitch angle
ϕ_0	-210	44	rad m^{-2}	[-1000, +1000]	Foreground RM
x_0	70	3	pc	[0, 100]	Offset in x
y_0	0		pc		Offset in y
z_0	-20		pc		Offset in z
n_0	10		cm^{-3}		Peak of GC electron density Gaussian
n_d	0.019		cm^{-3}		Electron density of disc
r_{GC}	8000		pc		Distance to GC
w	240		pc		Horizontal FWHM
h	125		pc		Vertical FWHM

^aThe range of parameter values allowed during the constrained nonlinear model fit. If no range is shown, the parameter is fixed.

$$fI d\vec{r} \propto n_e d\vec{r}. \quad (9)$$

We can now combine the polarized emissivity from Equation 9 with the Faraday depth and Faraday thickness to create the Faraday dispersion function $F(\phi)$. The dispersion function is the polarized flux as a function of Faraday depth, which can be Fourier transformed into the complex fractional polarization as a function of λ^2 (Brentjens & de Bruyn 2005). We assume that the intrinsic polarization angle is the same throughout the GC region, which is reasonable given the large-scale organization reported elsewhere (Nishiyama et al. 2010). The integration was done from $r_{\text{GC}} - 5w$ to $r_{\text{GC}} + 5w$ to predict the emission across the entire GC region. All lines of sight are normalized to have a polarization fraction of 70% at $\lambda^2 = 0$.

Figure 12 shows several predictions of the model given the assumptions described above. Since the initial model was fit assuming emission at the GC distance and RM induced only in the foreground of the GC (i.e., 2), we expect this model to be more Faraday thick. Indeed, while the underlying model is smooth and simple, the RM and polarization fraction are highly structured as a function of latitude and frequency. It is also worth noting that the predictions of the model are idealized in the sense that they do not account for beam depolarization or finite bandwidth of the observations. As such, they likely overpredict the polarization fraction and frequency-dependent changes in RM.

The relation between Faraday depth and physical distance is displayed in the top left panel of Figure 12. The Faraday depth changes little far from the GC because the medium is tenuous. However, it also changes little in dense regions where the field direction reverses, such as in front of and behind the GC. As a result, a significant amount of flux will end up at the Faraday depths of the vertical sections of the r versus ϕ plot. The flux *per unit* ϕ is large in these regions, as shown in the Faraday dispersion plot in the bottom left panel. Because these caustic-like features occur whenever the line-of-sight field reverses in a synchrotron emitting area (Ue-Li Pen, 2010, private communication), RM synthesis of Faraday thick areas is much more sensitive to these reversals than to the bulk emission at large ϕ scales.

If we think of the polarized emission as a complex Stokes vector that rotates according to its Faraday depth, we can imagine the effect on the observed RM. The peaks in $F(\phi)$ interfere to create complex Faraday effects as a function of λ^2 . As shown in the top right panel, the RM as determined by observing only two nearby frequencies can vary widely and argues for caution when interpreting our physical model. This shows that considering the emission from the entire GC region (not just the Faraday rotation by the foreground) makes the region Faraday thick.

Despite the Faraday thickness, the model shows that the RM at 6 cm preserves the observed east-west gradient. Figure 13 compares our observed RM at 6 cm to the RM derived along many lines of sight through this model. This is similar to the RM derived from the model in Figure 11, which did not calculate the Faraday dispersion function, but instead assumed Faraday rotation occurred in the foreground. Figure 13 confirms that considering the emissivity produces a wide range of RM, but that there is a clear east-west gradient.⁶ The qualitative agreement between models with and without emissivity shows that the observed RM gradient is caused by the orientation of the magnetic field in the GC region.

Figure 12 also shows the polarization fraction expected when considering the emissivity of the model. As we assume an intrinsic polarization fraction of 70%, the plot shows that nearly every line of sight will have significant depolarization. On average, the predicted polarization fraction is 20% at 4.8 GHz and 7% at 1.4 GHz. Since the simulation does not include beam depolarization and assumes a perfectly organized magnetic field, the predictions should overestimate the polarization fraction. We consider the predictions in agreement with the observed polarization fraction of 10 to 20% at 4.86 GHz and $< 1\%$ at 1.4 GHz.

In summary, considering the emissivity of our best-fit model for the GC magnetized plasma shows that the observed RM structure has a complex connection to the actual physical properties. However, the RM trend with Galactic longitude is directly related to the magnetic field

⁶ The observed RM matches the model in the east, but tends to be more positive than the model in the west. This shows that considering the emissivity and the full Faraday thickness requires more detailed modeling in the western part of the survey region.

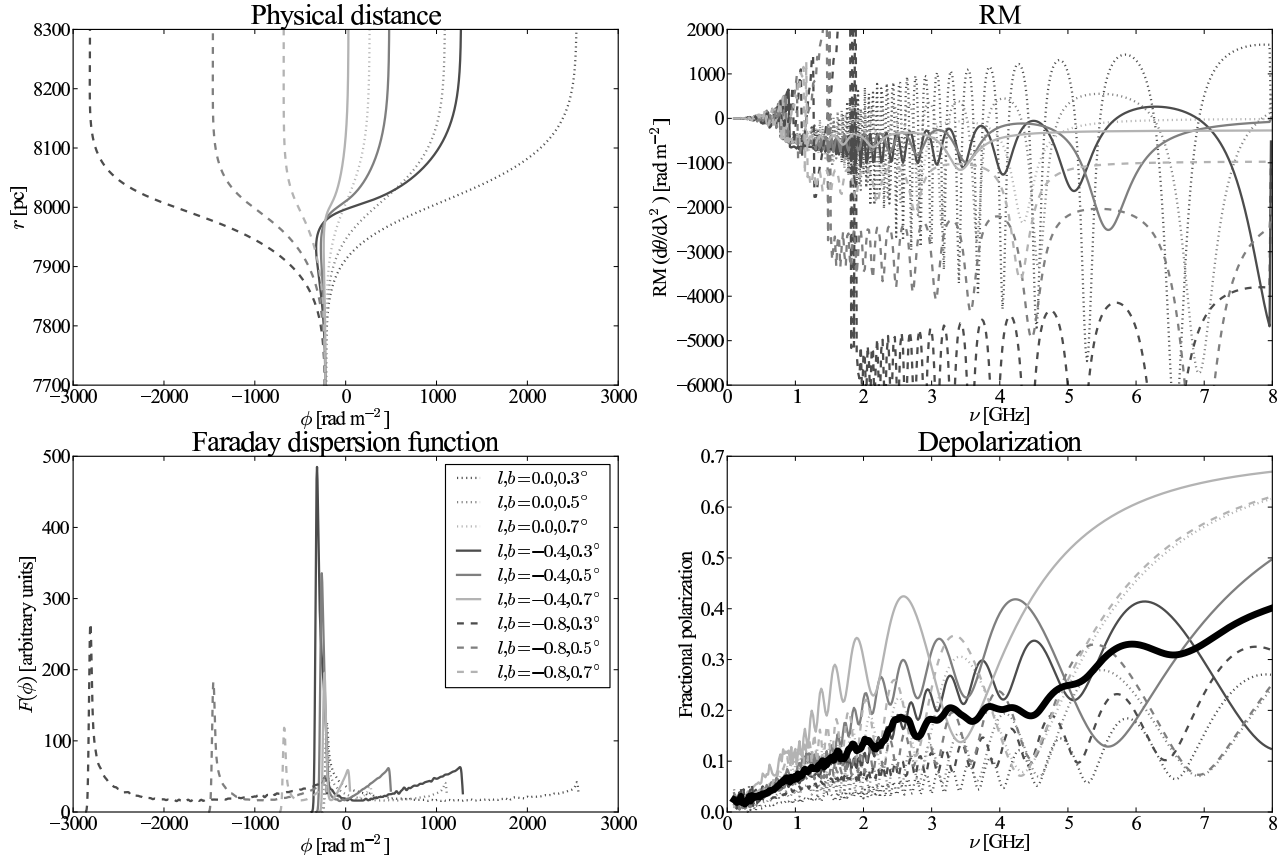


FIG. 12.— Observational predictions of the model. The legend at the bottom left is valid for all panels. *Top left*: Physical distance as a function of Faraday depth. *Bottom left*: Faraday dispersion function at same ϕ scale as top left. *Top right*: Slope of polarization angle versus λ^2 . *Bottom right*: Fractional polarization. The thick curve is the average of the other curves.

direction in the GC region. More detailed physical modeling will require polarimetry with hundreds of channels between 2 and 8 GHz, such as with the EVLA (Ulvestad et al. 2006).

5.2. Coincidence of RM for Extended and Filamentary Emission

Eight NRFs were detected in polarized emission at 6 cm and seven of these have reliable RM measurements (Law et al. 2008a). Interestingly, all but one of these have RM consistent with their surrounding diffuse emission. In other words, the RMs toward the NRFs largely follow the longitude dependence found toward the diffuse emission. If the RMs toward the filaments was unrelated to that of the diffuse emission, a binomial probability distribution predicts a 5% chance of 6/7 coincidences.

The similarity of the RMs in the diffuse and filamentary emission is consistent with observations of the brightest NRF, the Radio Arc. As shown in § 3.2 and elsewhere (Yusef-Zadeh & Morris 1988), the morphology and RM measured toward the Radio Arc has a continuous connection into the polarized diffuse emission in the east of this survey. Since the Radio Arc is known to be within the central 100 pc of the GC (Yusef-Zadeh & Morris 1987; Lang et al. 1999b; Lasenby et al. 1989), some of the diffuse polarized emission must also be located in the GC.

The fact that the filaments and the diffuse polarized emission are physically near each other could explain

their similar RMs. The simplest model to explain this coincidence is that the filaments and diffuse emission are behind the same Faraday screen. According to our modeling, such a screen would be located within the central kiloparsec. However, NRFs are known to have RM changes that coincide with physical changes, which argues that some RM is induced locally (Lang et al. 1999a). A locally induced RM is consistent with the strong magnetic fields inferred in NRFs (Yusef-Zadeh et al. 1997).

If this RM coincidence is not extrinsic, then it must be intrinsic: the diffuse emission and the NRFs have similar magnetic field orientations. Physically, this can be explained if the NRFs are local enhancements and perturbations of the global magnetic field. This concept is common to several models for generating NRFs (e.g., Benford 1988; Serabyn & Morris 1994; Boldyrev & Yusef-Zadeh 2006). However, it excludes the model of Shore & LaRosa (1999), which relies on an interaction of molecular clouds with a global wind to generate the NRFs. Other models (e.g., Rosner & Bodo 1996) do not clearly predict how filaments can enhance and perturb the global magnetic field.

The NRFs and the diffuse polarized emission also have a similar spatial distribution. As described earlier, the RM observed in the diffuse emission changes sign near $l \approx -0^\circ 35'$. Other observations, described in § 5.3, show that most RM measurements in the GC region follow a pattern that is centered near $l \approx -0^\circ 35'$. High-resolution

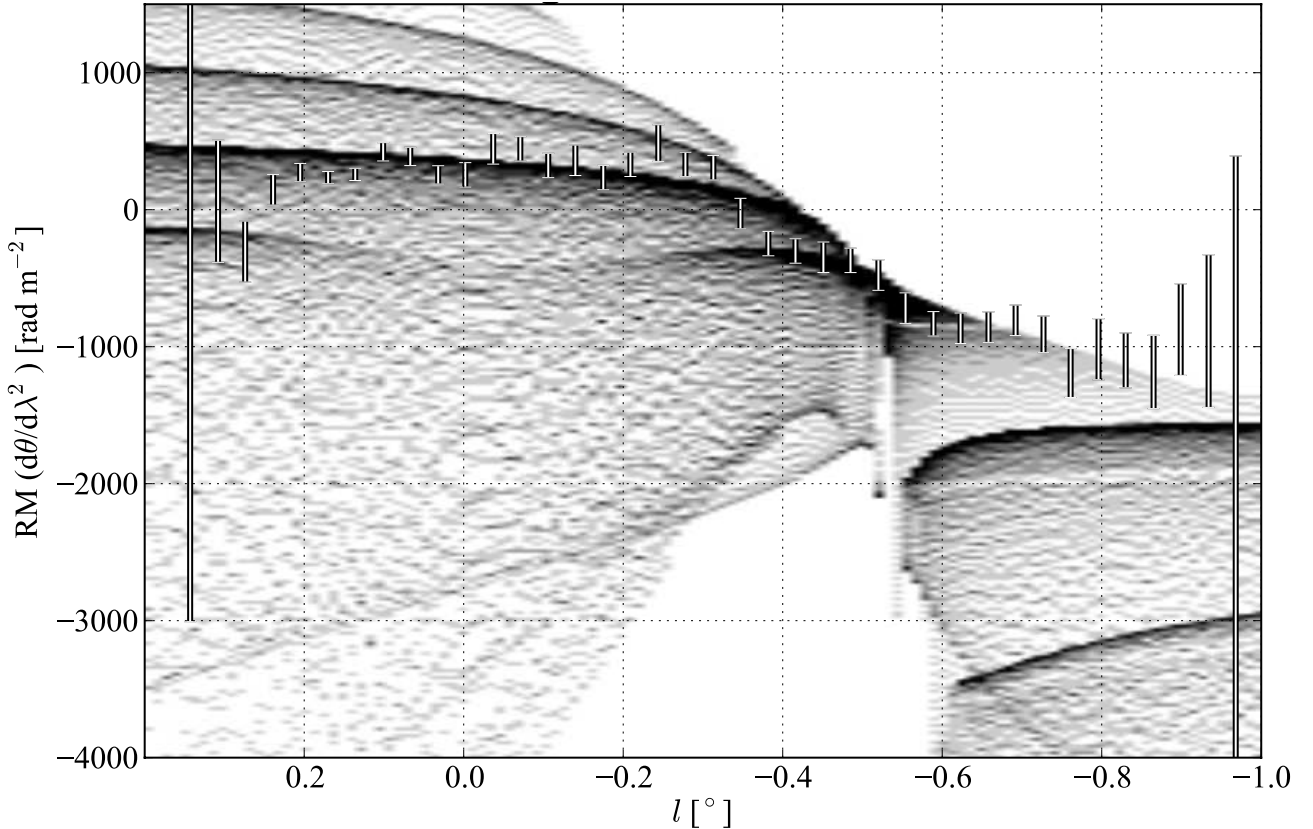


FIG. 13.— Comparison of the predicted and observed RM at 4.86 GHz (near 6 cm) as a function of Galactic longitude. The gray scale shows RM values expected for lines of sight with b ranging from $0^{\circ}2$ to $0^{\circ}7$. The prediction was made using the model shown in Tab. 1 and considering the emission and Faraday rotation through the entire GC region. The vertical bars show the observed RM at 4.86 GHz, as shown in Fig. 7.

20 cm survey of Yusef-Zadeh et al. (2004) showed that there are dozens of candidate NRFs in the GC region with the highest density between $l = 0^{\circ}2$ to $-0^{\circ}7$. This shows that the center of the distribution of NRFs is similar to the center of the RM pattern. A third coincidence is that the GC lobe, a shell of gas related to a mass outflow, is centered near the same longitude. These coincidences indicate a connection between the GC lobe outflow and the GC magnetic field.

5.3. Degree-Scale Structure in the GC Magnetic Field

Figure 14 shows a schematic of all RM measurements toward sources believed to be in or beyond the GC region. The RM values derived earlier in this work are shown along with observations of the extended polarized emission from the Radio Arc (Tsuboi et al. 1986), other NRFs (Lang et al. 1999a,b; Gray et al. 1995; Reich 2003), and background sources (Roy et al. 2005). North of the plane, the east-west gradient in RM is seen toward diffuse, compact, and filamentary sources. The pattern is antisymmetric about $l \approx -0^{\circ}35$ and across the Galactic plane (esp. Tsuboi et al. 1986).

The simplest pattern to describe the GC RM values is that of a checkerboard (four quadrants of alternating sign) shifted $0^{\circ}35$ (≈ 50 pc) west of the center. The pos-

sibility of a checkerboard pattern centered at $l = 0^{\circ}$ has been noted before (Uchida et al. 1985; Novak et al. 2003), but some RM values were not consistent with the pattern (Ferrière 2009). The RM reported in this work finds that the checkerboard pattern is robust if it is assumed to be shifted from the center.

The checkerboard pattern inspired the “flux-dragging” model for the GC magnetic field (Uchida et al. 1985; Novak et al. 2003). The model explains a large-scale pattern in the GC RM as the effect of Galactic rotation on a frozen-in, poloidal (vertical) magnetic field. As the disk rotates, the magnetic field in the disk is dragged away from us on the east side and toward us on the west side. This pull creates a line-of-sight component of the magnetic field. This perturbation to the magnetic field has a checkerboard pattern in the sign of the RM, such that the RM will have opposite signs toward any two adjacent quadrants formed about the center of rotation.

Interestingly, the parity of the checkerboard pattern constrains the orientation of the magnetic field, breaking the 180° ambiguity of observations of the polarization angle. If this scenario is valid, the parity of the observed pattern is consistent with the magnetic field pointing from south to north. This is the only known measurement that can break this ambiguity in the orien-

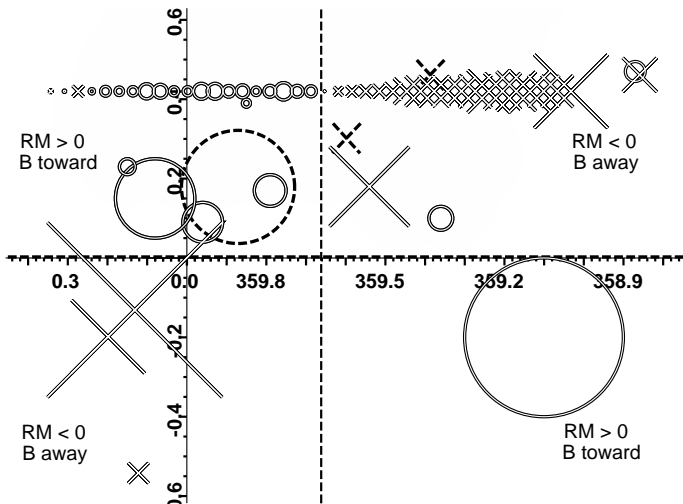


FIG. 14.— Schematic diagram of measurements of RM in the central degree of the Galaxy. The cross symbols show sources with negative RM and circles show sources with positive RM. The size of the symbol is proportional to the value of RM, with values ranging from 1100 to -2200 rad m^{-2} . The horizontal series of symbols show the RM averaged over all latitudes of the present survey. The other solid-lined symbols show measurements from the literature, specifically: G0.08+0.15 (a.k.a. “the Northern thread” Lang et al. 1999b), the Radio Arc (south of $b = 0^\circ$; Tsuboi et al. 1986), G0.87–0.87 (Reich 2003), G359.1–0.2 (a.k.a. “the Snake”; Gray et al. 1995), G358.85+0.47 (a.k.a. “the Pelican”; Lang et al. 1999a), and new filaments described in Law et al. (2008a). Note that the two symbols furthest to the top-right represent the max and min RM measured toward the unusual “Pelican” NRF. The dashed crosses and circles show the RM measured toward extragalactic sources (Roy et al. 2005). The dashed horizontal and vertical lines split the region into quadrants that mostly have similar RM values.

tation of the magnetic field on the plane of the sky.

Roy et al. (2008) found that the flux-dragging scenario was inconsistent with the RM observed toward extragalactic sources seen through the central 12° . The RM toward their 60 background sources had an average $\text{RM} = +413 \text{ rad m}^{-2}$ and no checkerboard pattern. While the the RM values over the central 12° are predominantly positive, the three measurements in the central 2° studied here (G359.388+0.460, G359.604+0.306, G359.871+0.179) agree with the shifted checkerboard pattern.

However, there are clear differences between the RM structure seen here and that reported by Roy et al. (2008). For example, the average RM observed by Roy et al. (2008) in the central 12° is not consistent with the foreground RM in our model (ϕ_0). Assuming that half of the average RM is contributed by the foreground to the GC, we’d expect $\phi_0 = 206.5 \text{ rad m}^{-2}$, but find roughly the opposite of that. One possibility is that the foreground RM fit by our model is poorly constrained by our data. Indeed, §5.1.3 shows that the absolute level of RM is poorly constrained by these narrow-band observations, but that relative values are well constrained. Another possibility is that the central 2 degrees of the Galaxy is magnetically and dynamically different from the region beyond, making comparison with the RM measured in Roy et al. (2008) less meaningful. The presence of NRFs (Nord et al. 2004; Yusef-Zadeh et al. 2004) and the “central molecular zone” (Morris & Serabyn 1996) makes the central 2° notably different from the region beyond.

In summary, we argue that RM measured in the central

2° of the Galaxy is distinct from RM structure seen outside this region and that it reflects large-scale GC magnetic field structure. The RM structure is simplest to describe as a checkerboard pattern shifted $\sim 50 \text{ pc}$ from the dynamical center of the Galaxy. The longitude shift requires some non-Keplerian motion of the ionized gas in the GC region. This is consistent with recent observations showing that the GC is host to a small starburst outflow centered $\sim 50 \text{ pc}$ west of the GC (the GC lobe; Bland-Hawthorn & Cohen 2003; Law 2010). The distribution of NRFs, a more direct tracer of the GC magnetic field, is also centered tens of parsecs west of the GC (see Figure 29 of Yusef-Zadeh et al. 2004). It is clear that the electron and magnetic field distributions are not symmetric about the $l = 0^\circ$; our new RM measurements confirm this.

6. CONCLUSIONS

We have presented observations and modeling of polarized 6 cm radio continuum emission toward 0.5 square degrees of the GC region. The radio continuum survey detects polarized emission throughout the region in the form of diffuse polarized emission, compact sources, and filamentary sources. The two bands in the continuum observations allow us to measure RM to this polarized emission. We develop a statistical technique to measure the RM; comparing our results to more robust RM measurements shows that our technique is reliable.

There is a striking large-scale pattern in RM toward the diffuse polarized emission. Values in the eastern part of the survey are generally about $+330 \text{ rad m}^{-2}$, but change to -880 rad m^{-2} in the western part of the survey. There is a sharp transition around $l = -0^\circ.35$ at all latitudes in the survey. Modeling of the propagation of the polarized signal shows that this pattern is induced within $\sim 1 \text{ kpc}$ of the GC region. The RM measured toward radio filaments known to be in the GC region are generally consistent with that of the diffuse polarized emission. This coincidence is consistent with models for the filaments as localized enhancements to a global magnetic field.

The modeling of the GC magnetized plasma shows that the RM structure constrains the orientation of the GC magnetic field. This RM pattern shows that the GC magnetic field is organized on size scales of roughly 150 parsecs. Combining these and other RM measurements in the GC region, we strengthen earlier suggestions for a checkerboard pattern in RM covering the central 300 parsecs, but only if the structure is shifted roughly 50 pc west of the dynamical center of the Galaxy. We show that the RM measured along different lines of sight and toward different tracers are consistent with this shift.

The observed polarization and RM in the GC is consistent with the GC having a poloidal magnetic field that is perturbed by the motion of gas in the Galactic disk (Uchida et al. 1985; Novak et al. 2003). This model is being supported by a growing body of evidence (Chuss et al. 2003; Nishiyama et al. 2010). Under this model, our RM observations constrain the GC magnetic field to be directed from south to north. Our observations also suggest that a second-order perturbation, a small outflow from the GC, has shifted the magnetic symmetry axis of the GC about 50 pc west of the dynamical center of the Galaxy.

New observations can test this model in several ways. First, observing the diffuse polarized emission between 6 and 20 cm (5 and 1.4 GHz), where it becomes Faraday thick, would constrain models of its physical distribution. Expanded VLA observations with thousands of channels at these frequencies will track the Faraday rotation and depolarization well enough to create a 3D reconstruction of the magnetic field topology in the Galactic Center. Second, measuring the RM of other radio filaments would test the idea that they are preferentially aligned with the RM of the extended polarized emission. Third, the

detection of diffuse polarized emission and its RM beyond the region studied here (particularly south of the plane) would confirm that it traces a general property of the GC region.

We thank Farhad Yusef-Zadeh, Bryan Gaensler, Bill Cotton, and Dominic Schnitzeler for valuable discussions during this work.

Facilities: VLA

APPENDIX

SPATIALLY SMOOTHING $\Delta\theta$

Mean $\Delta\theta$ Images

To improve visualization of the $\Delta\theta$ images, the mosaics were smoothed using two independent methods. Both methods were implemented in IDL. The first method of smoothing $\Delta\theta$ was to measure the error weighted mean value of $\Delta\theta$ over small regions. Hereafter, we refer to this as the mean method.

A major caveat to this method is that averaging angles is not proper, since they represent vector quantities. However, averaging angles is approximately correct for small angles, which is usually true for the $\Delta\theta$ images presented here (Fig. 4). Furthermore, the large values in the $\Delta\theta$ map are generally in the noisiest parts of the image and are down-weighted by large errors. There was no significant difference when using the median instead of the mean.

Fitting Histograms of $\Delta\theta$ Images

A second, more robust method of smoothing the $\Delta\theta$ images is to fit the distribution of $\Delta\theta$ values with a model. Since a model is fit to the histogram, this approach avoids the problems of averaging angles. The model can also parameterize the noise- and signal-like contributions to the $\Delta\theta$ distribution, making it robust to outliers.

As described in §3.1, histograms of $\Delta\theta$ were fit with a Lorentzian plus a constant background. The best-fit values and their errors were found by the Levenberg-Marquardt algorithm, implemented as MPFIT in IDL (Markwardt 2009). All errors reported are 1σ confidence intervals.

Figure 4 shows two examples of histograms extracted with best-fit models. A histogram bin size of 2.5° was used; varying the bin size by a factor of a few does not significantly change the fit. The smoothed maps have pixel sizes of $125'' \times 125''$, which are small enough to resolve structure in the mosaic, but large enough for accurate fit results.

An advantage of the histogram-fitting method is that it calculates the mean and error in $\Delta\theta$ from the distribution of $\Delta\theta$; no noise image is required. A disadvantage of the histogram-fitting method is that it assumes that all pixels in the region sampled are a part of the same distribution. In fact, there are times when multiple sources, with different distributions of $\Delta\theta$ (i.e., different RMs) are sampled by the same histogram. In this case, the source that occupies the most pixels will dominate the histogram distribution and the best-fit value of $\Delta\theta$. This is different from what happens when calculating an error-weighted average of $\Delta\theta$, in which the average is dominated by the pixels with the lowest noise (i.e., the brightest sources).

Comparing Mean and Histogram-Fitting Methods

Figure A1 compares images of $\Delta\theta$ using the mean and histogram-fitting methods for a grid of $125''$ boxes. An image showing the significance of differences between the two methods in each pixel. The average difference between the two images is 0.002° and the standard deviation is about 0.2° , so there is no significant difference between the two methods.

The image showing the difference in the two smoothing methods highlights two regions with greater than 1σ : $(359^\circ55, 0^\circ15)$ and $(0^\circ15, 0^\circ2)$. These differences demonstrate the biases of the methods. In both locations, there is a small, polarized source with a different $\Delta\theta$ from the large, polarized background. Since the mean method favors bright sources and the histogram-fitting method favors large sources, these two regions are most likely to show a difference. While this is an important caveat, Figure A1 shows that, in general, the two methods are in good agreement.

The errors on $\Delta\theta$ differ according to the method used. When averaging over 125 -arcsec tiles, both methods give errors within 50% of each other, if errors $< 3^\circ$. However, for errors greater than 3° , the errors found with the mean method are progressively less than those found by histogram fitting. The maximal error found by the mean is about 20° , while the histogram-fitting method has a maximal error of about 200° . This is expected, since the mean method assumes that angles are much smaller than 1 rad; this is not always true for the errors in $\Delta\theta$. Thus, the histogram fitting errors are a more accurate and more conservative estimate of the true errors in the mean value of $\Delta\theta$.

REFERENCES

- Benford, G. 1988, ApJ, 333, 735
 Bland-Hawthorn, J & Cohen, M. 2003, ApJ, 582, 246
 Boldyrev, S. & Yusef-Zadeh, F. 2006, ApJ, 637, L101
 Brentjens, M. & de Bruyn, A. G. 2005, A&A, 441, 1217
 Burn, B. J., 1966, MNRAS, 133, 67
 Chuss, D. T., Davidson, J. A., Dotson, J. L., Dowell, C. D., Hildebrand, R. H., Novak, G., & Vaillancourt, J. E. 2003, ApJ, 599, 1116

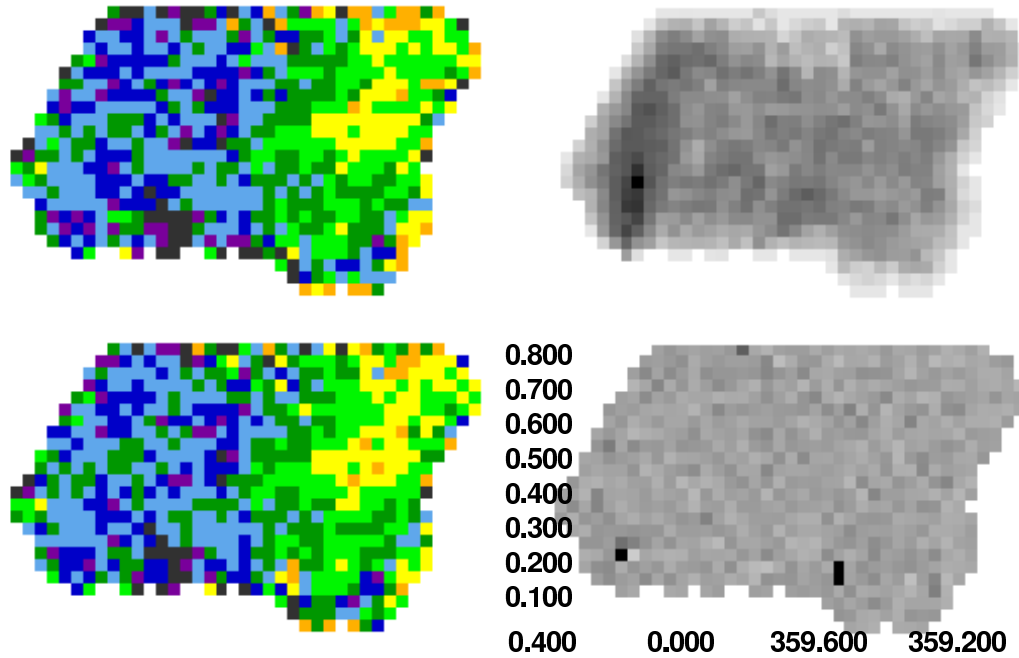


FIG. A1.— *Top left*: Smoothed map of $\Delta\theta$ for the entire survey region with $125'' \times 125''$ tiles after using the histogram-fitting method. The color-scale shows colors of light blue through purple representing negative $\Delta\theta$ and colors from yellow through red representing positive $\Delta\theta$. *Top right*: Map of the error in $\Delta\theta$ for the image shown in the top left. The values range from $0''.08$ to $20''$. *Bottom left*: Smoothed map of $\Delta\theta$ as in the top left panel when using the mean method. *Bottom right*: Map of the difference significance between the histogram-fitting and mean methods with values ranging from -1σ to $+1\sigma$.

- Cordes, J. M. & Lazio, T. J. W. 2002, astro-ph/0207156
 Cotton, W. D. 1994, AIPS memo 86, <http://www.aips.nrao.edu/aipsmemo.html>
 Cotton, W. D. 1999, Synthesis Imaging in Radio Astronomy II, ASP, 180, 120
 Crocker, Roland M., Jones, David I., Melia, Fulvio, Ott, Jrgen, & Protheroe, Raymond J. 2010, Nature, 463, 65
 Ferrière, K. 2009, A&A, 505, 1183
 Gaensler, B. M., Madsen, G. J., Chatterjee, S., & Mao, S. A. 2008, PASA, 25, 184
 Gehrels, N. 1986, ApJ, 303, 336
 Gray, A.D., Nicholls, J., Ekers, R. D., & Cram, L. E. 1995, ApJ, 448, 164
 Han, J. L., Manchester, R. N., Lyne, A. G., Qiao, G. J., van Straten, W. 2006, ApJ, 642, 868
 Haverkorn, M., Katgert, P., & de Bruyn, A. G. 2004, A&A, 427, 549
 Haynes, R. F., Stewart, R. T., Gray, A. D., Reich, W., Reich, P., & Mebold, U. 1992, A&A, 264, 500
 Lang, C. C., Anantharamaiah, K.R., Kassim, N.E., & Lazio, T. J. W. 1999, ApJ, 521, L41
 Lang, C. C., Morris, M., Echevarria, L. 1999, ApJ, 526, 727
 LaRosa, T. N., Brogan, C. L., Shore, S. N., Lazio, T. J., Kassim, N. E., & Nord, M. E. 2005, ApJ, 626, L23
 LaRosa, T. N., Lazio, T. J. W., & Kassim, N. E. 2001, ApJ, 563, 163
 LaRosa, T. N., Shore, S. N., Lazio, T. J. W., & Kassim, N. E. 2006, JPhCS, 54, 10
 Lasenby, J., Lasenby, A. N., & Yusef-Zadeh, F. 1989, ApJ, 343, 177
 Law, C. 2010, ApJ 708, 474
 Law, C., Yusef-Zadeh, F., & Cotton, W. D. 2008, 177, 515
 Law, C., Yusef-Zadeh, F., Cotton, W. D., & Maddalena, R. 2008, 177, 255
 Lazio, T. J. W. & Cordes, J. M. 1998, ApJ, 505, 715
 Manchester, R. N., Hobbs, G. B., Teoh, A. & Hobbs, M. 2005, AJ, 129, 1993
 Markwardt, C. B. 2009, ASPC, 411, 251
 Morris, M. & Serabyn, E. 1996, ARA&A, 34, 645
 Murgia, M., et al. 2004, A&A, 477, 573
 Nishiyama, et al. 2010, ApJ, 722, L23
 Nord, M. E., Lazio, T. J. W., Kassim, N. E., Hyman, S. D., LaRosa, T. N., Brogan, C. L., & Duric, N. 2004, AJ, 128, 1646 (erratum 131, 1886, [2006])
 Novak, G., et al. 2003, ApJ, 583, L83
 Plante, R. L., Lo, K. Y., & Crutcher, R. M. 1995, ApJ, 445, L113
 Reich, W. 2003, A&A, 401, 1023
 Roelfsema, P. R., Goss, W. M., & Geballe, T. R. 1989, A&A, 222, 247
 Rosner, R.; Bodo, G. 1996, ApJ, 470L, 49
 Roy, S., Rao, A. P., & Subrahmanyam, R. 2005, MNRAS, 360, 1305
 Roy, S., Rao, A. P., & Subrahmanyam, R. 2008, A&A, 478, 435
 Rudnick, L. & Brown, S. 2009, AJ, 137, 145
 Sault, R. J., Hamaker, J. P., & Bregman, J. D. 1996, A&AS, 117, 149
 Schnitzeler, D.H.F.M., Katgert, P., & de Bruyn, A.G. 2009, A&A, 494, 611
 Serabyn, E. & Morris, M. 1994, ApJ, 424L, 91
 Shore, S. N. & LaRosa, T. N. 1999, ApJ, 521, 587
 Sofue, Y. & Handa, T. 1984, Nature, 310, 568
 Spangler, S. R. 1991, ApJ, 376, 540
 Sun, X. H., Reich, W., Waelkens, A., & Ensslin, T. A. 2008, A&A, 477, 573
 Taylor, A. R., Stil, J. M., & Sunstrum, C. 2009, ApJ, 702, 1230
 Tsuboi, M., et al. 1986, AJ, 92, 818
 Uchida, Y., Shibata, K., & Sofue, Y. 1985, Nature, 317, 699
 Ulvestad, J. S. et al. 2006, BAAS, 208, 5501
 Wieringa, M. H., de Bruyn, A. G., Jansen, D., Brouw, W. N., & Katgert, P. 1993, A&A, 268, 215
 Yusef-Zadeh, F. & Morris, M. 1987, ApJ, 320, 545
 Yusef-Zadeh, F. & Morris, M. 1988, ApJ, 329, 729
 Yusef-Zadeh, F., Morris, M., & Chance, D. 1984, Nature, 310, 557
 Yusef-Zadeh, F., Hewitt, J., & Cotton, W. 2004, ApJS, 155, 421
 Yusef-Zadeh, F., Wardle, M., & Parastaran, P. 1997, ApJ, 475, L119
 Yusef-Zadeh, F., Morris, Mark, Slee, O. B., & Nelson, G. J. 1986, ApJ, 310, 689
 Zhu, C., Byrd, R. H., Lu, P. & Nodcal, J. 1994, L-BFGS-B - Fortran Subroutines for Large-Scale Bound Constrained Optimization, Tech. rep., ACM Trans. Math. Software